

Computer Vision Based Hairline Mandibular Fracture Detection from Computed Tomography Images

Ananda S. Chowdhury, Anindita Mukherjee, Suchendra M. Bhandarkar, and Jack C. Yu

Abstract This chapter addresses the problem of detection of hairline mandibular fractures from a sequence of computed tomography (CT) images. It has been observed that such a fracture can be easily overlooked during manual detection due to the absence of sharp surface and contour discontinuities and the presence of intensity inhomogeneity in the CT images. In this work, the 2D CT image slices of a mandible with hairline fractures are first identified from the input sequence of a fractured craniofacial skeleton. Two intensity-based image retrieval schemes with different measures of similarity, namely the Jaccard index and the Kolmogorov–Smirnov distance, are applied for that purpose. In the second part, we detect a hairline fracture in the previously identified subset of images using the maximum flow–minimum cut algorithm. Since a hairline fracture is essentially a discontinuity in the bone contour, we model it as a minimum cut in an appropriately weighted flow network constructed using the geometry of the human mandible. The Ford–Fulkerson algorithm with Edmonds–Karp refinement is employed to obtain a minimum cut. Experimental results demonstrate the effectiveness of the proposed method.

A.S. Chowdhury (✉)

Department of Electronics and Telecommunication Engineering, Jadavpur University, Kolkata 700032, India

e-mail: aschowdhury@etce.jdvu.ac.in

A. Mukherjee

Department of Computer Science, Dream Institute of Technology, Kolkata 700104, India

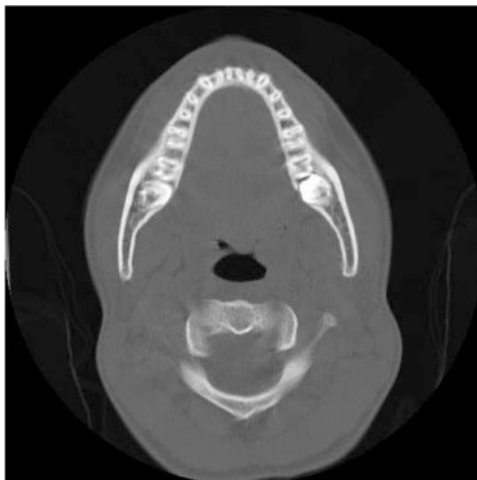
S.M. Bhandarkar

Department of Computer Science, University of Georgia, Augusta, GA 30912, USA

J.C. Yu

Department of Plastic Surgery, Georgia Health Sciences University, Athens, GA 30602, USA

Fig. 1 CT scan of an unbroken mandible



1 Introduction

Craniofacial fractures are very frequently encountered in modern society, the principal reasons being gunshot wounds, motor vehicle accidents, and sports related injuries [1]. Ogundare et al. [2] in their research illustrated that the fracture patterns sometimes imply a single fracture, and, in some other cases, there can be a combination of single fractures. The craniofacial skeleton consists of high stress-bearing buttresses and low stress-bearing curve planes. When external loads are applied, the craniofacial skeleton undergoes strain. When the strain exceeds the ultimate strain limit, failure occurs [3]. The resulting loss of spatial continuity in the craniofacial skeleton is clinically termed as fracture which causes pain, disfigurement, and functional impairment due to the disruption of force transmission. In some situations, the broken fragments may suffer negligible relative displacement. They are termed as hairline/minor fractures. For the purpose of illustration, we first show a 2D slice of an intact human mandible in Fig. 1. A typical hairline/minor fracture is presented in Fig. 2.

The input to our problem is a sequence of computed tomography (CT) images with scans of human craniofacial skeleton. A typical sequence consists of many slices out of which only a handful is observed to contain the fractured mandible. Figure 3 shows a typical input sequence.

Note that not all four slices in Fig. 3 contain the fractures. A careful scrutiny reveals that only the two middle slices have these fractures. So, we decide to first retrieve only the fracture containing slices from the entire input sequence. This is achieved using two intensity-based image retrieval approaches [4] with Jaccard index and Kolmogorov–Smirnov distance as measures of similarity. We next apply

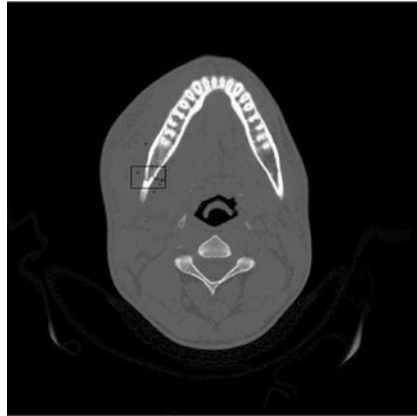


Fig. 2 CT scan of a mandible with a minor fracture (within the *black rectangle*)

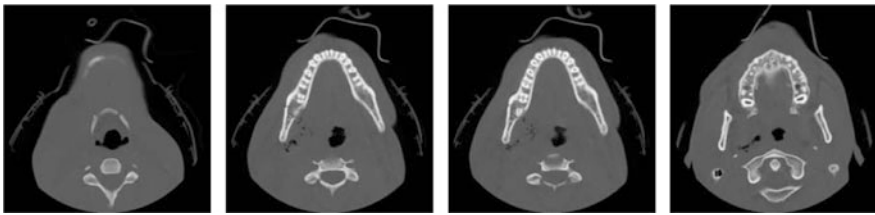


Fig. 3 An input sequence with four different slices

the max-flow min-cut algorithm to only the above fracture containing slices. A flow network with appropriate weights is constructed following the geometry of the mandible. A fracture is modeled as a minimum cut in such a network. The Ford–Fulkerson [5] algorithm is applied for the detection of a minimum cut. To expedite the Ford–Fulkerson algorithm, the augmenting paths are detected using breadth-first search, as indicated by Edmonds–Karp [6]. The overall goal is to develop an enabling technology that leverages the advances in computer vision to detect hairline mandibular fractures. The work presented here can be of good help for practicing radiologists and surgeons.

The rest of this chapter is organized in the following manner. In Sect. 2, we provide the state-of-the-art and highlight our contribution. Section 3 is devoted to the intensity-based image retrieval methods. In Sect. 4, we describe the max-flow min-cut based fracture detection. Experimental results are presented in Sect. 5. The chapter is concluded in Sect. 6 with an outline of future directions of research.

2 Literature Review

While there exists recent work published in the literature dealing with simulation of mandibular fractures [7], and simulation of dental implants [8]; only a little has been reported about computer-aided detection of craniofacial fractures. The relative paucity of existing literature on automated mandibular surgery has made us interested in carrying out this important research work.

Detection of well-displaced mandibular fractures, wherein the broken fragments have undergone noticeable relative displacement, using a Bayesian inference approach has been reported in a previous work by Chowdhury et al. [9]. A Markov random field (MRF)-based approach for detection of mandibular hairline fractures has been also presented by Chowdhury et al. [10]. However, the MRF-based scheme is computationally intensive. Furthermore, the MRF-based scheme is based on an underlying assumption that the bilateral symmetry of a mandible is preserved in the case of a hairline fracture, which may not necessarily hold in some cases.

In this paper, the 2D CT slices containing a fractured mandible are first identified within the entire CT image sequence of a fractured craniofacial skeleton using the Jaccard index and the Kolmogorov–Smirnov (KS) distance measures. Within each identified 2D CT slice, a hairline fracture is modeled as a *cut* in the flow of image intensities along the bone contours. The flow is conceived between two anatomical landmark points on the human mandible, called condyles [11]. The geometry of the mandibular contours is used to construct the flow network. In graph theory, this is equivalent to finding a minimum cut in the flow graph between the *source* and the *sink* vertices. It is important to note that unlike the MRF-based scheme in [10], the proposed method is computationally fast and does not rely on the assumption of preservation of bilateral symmetry for mandibles with hairline fractures. A part of the work described here has been published in [12].

3 Retrieval of Fracture Containing Slices

Content-based image retrieval (CBIR) consists of retrieving the most visually similar images to a given query/reference image from a database of images. The ever-increasing number of digital images in the medical domain has amplified the need for automated search and retrieval tools. For an excellent survey in this subject, see the work by Müller et al. [4]. Rahman et al. [13] proposed a CBIR framework for diverse collection of medical images of different imaging modalities and anatomic regions with different orientations. In another paper, Selvarani and Annadurai [14] discuss general Fourier descriptor (GFD) for shape representation for the purpose of medical image retrieval. Sedghi et al. [15] discuss the relevance criteria for searching of various medical images.

In the present problem, an intact mandible serves as the query/reference image and the candidate slices in any input sequence constitute the database of images. We propose two methods which are based on a general assumption that similar-looking

images should exhibit similar intensity patterns. The areas of high intensity and low intensity in an image can constitute important features because they often mark relevant image objects. As mandible is a bony structure, it typically exhibits considerably high intensity values compared to other components like soft tissues. We exploit these contrasting intensity patterns of the CT scans for retrieving slices containing the mandibles.

3.1 Image Pre-processing

We initially apply the following three image-processing tasks prior to intensity-based retrieval [16]:

1. Entropy thresholding
2. Median filtering
3. Histogram construction

3.1.1 Entropy Thresholding

In the CT data, the selection of the appropriate threshold is not obvious since the CT images typically contain objects or artifacts of different intensities (varying Hounsfield unit values). For example, a fractured mandibular fragment could contain cavities, dental fillings, crowns, and other dental prostheses. Thus, entropy-based thresholding [17] is chosen over simple thresholding. In the case of entropy-based thresholding, the threshold value is determined via maximization of the interclass entropy computed from the grayscale histogram of an image. For an image, the entropy S_c for each graylevel class c (consisting of several gray level values) can be computed using the grayscale histogram in the following manner:

$$S_c = - \sum_{k \in G_c} p(k) \log_2 (p(k)) \quad (1)$$

where $p(k)$ is the probability of a pixel having a grayscale value k and G_c is the set of graylevels for class c . In the context of binarization, the graylevel threshold T is chosen such that the total entropy $S = S_1 + S_2$ is maximized.

In Fig. 4, we show the image of the intact mandible. Result of entropy thresholding on that image is shown in Fig. 5.

3.1.2 Median Filtering

Median filter is a nonlinear digital filtering technique, often used to remove noise from images or other signals. Note that the filter could have been applied before the

Fig. 4 CT scan of an unbroken mandible

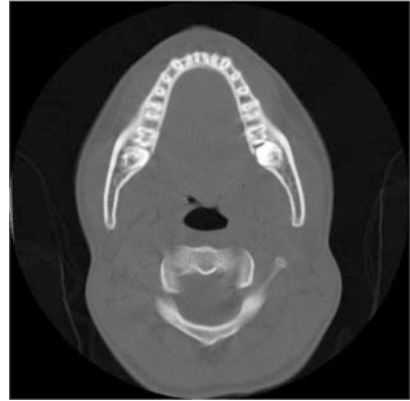


Fig. 5 Result of entropy thresholding in Fig. 4



entropy thresholding also. Here, we have applied the same after the thresholding is performed.

In Fig. 6, we show the result of median filtering on the image in Fig. 5.

3.1.3 Histogram Construction

In an image-processing context, the histogram of an image normally refers to a histogram of the pixel intensity values. The histogram is a graph that shows the number of pixels in an image at each different intensity value found in that image (Fig. 7).

3.2 Set-Based Approach and Choice of Similarity Measure

In this section, the set-based representation of an image is discussed along with the choice of *Normalized Jaccard Index (NJI)* as the measure of similarity. An image



Fig. 6 Result of median filtering in Fig. 5

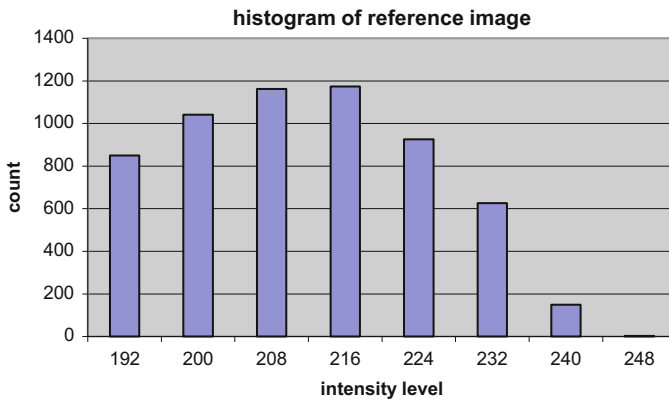


Fig. 7 Histogram of the image shown in Fig. 4. Only top 25 % intensities, i.e. values in the range 192–255 are considered

can be represented as a mathematical function over some finite domain. In general, we can represent that function f as $f:(x, y) \rightarrow z$ where $x, y, z \in R$ and R is the set of real numbers. The ordered pair (x, y) for an image represents spatial coordinates of a pixel with respect to some reference frame and z is the intensity value at that pixel location. For an n -bit grayscale image, $R = [0, 2^n - 1]$ and for a binary image $R = [0, 1]$. Now, we define union and intersection between two binary images $f(x, y)$ and $g(x, y)$.

Definition 1 If at a certain pixel location (x, y) , either $f(x, y)$ is 1 or $g(x, y)$ is 1, then the **union** between the two sets $f(x, y) \cup g(x, y) = 1$, else $f(x, y) \cup g(x, y) = 0$.

Definition 2 If at a certain pixel location (x, y) , both $f(x, y)$ and $g(x, y)$ are 1, then the **intersection** between the two sets $f(x, y) \cap g(x, y) = 1$, else $f(x, y) \cap g(x, y) = 0$.

Definition 3 **Jaccard index** is defined as follows:

$$J = \frac{|f(x, y) \cap g(x, y)|}{|f(x, y) \cup g(x, y)|} \quad (2)$$

In Eq. (2), the symbol “|” denotes cardinality of a set. Note that when $f(x, y)$ and $g(x, y)$ are two disjoint sets, which in this context means there is no overlap between the two binary images, $J = 0$. In contrast, when $f(x, y) = g(x, y)$, which in this context means two binary images completely overlap, $J = 1$. For partial overlap, J will assume appropriate intermediate values between 0 and 1. Among other related measures [18], both *Dice coefficient* and *Cosine coefficient* give more weight to the intersection part. We decide to give equal emphasis to intersection and union terms and hence choose *Jaccard index*.

3.3 Method-I: Image Retrieval Using Normalized Jaccard Index

Now, we describe our first method (method-I) for the image retrieval. Here, we compute the overlap between the reference image (i.e., unbroken mandible) and the candidate images (2D slices in any input sequence). The rationale behind the method is that two similar images exhibit a higher value of the overlap compared to two dissimilar images.

Figure 8 shows the flowchart for the first retrieval method. While computing the *Jaccard index*, we do not consider the entire images of dimensions $W \times H$. Here, W denotes the width of the image and H denotes the height of the image. We use a smaller area $w \times h$ instead, where $w < W$ and $h < H$. This selection of smaller area is based on our domain knowledge. After studying large number of slices, we came to conclusion that a mandible typically appears within a centrally located smaller region in the CT scans. Selection of a smaller area of interest increases the speed of *Jaccard index* computation (Fig. 9).

We normalize the value of the *Jaccard index* by dividing it with the maximum value for a given sequence. Normalization refers to the division of multiple sets of data by a common variable in order to negate that variable’s effect on the data, thus allowing underlying characteristics of the datasets to be compared. We finally threshold the *NJI* values to retrieve appropriate slices. Slices possessing values above the chosen threshold are retrieved.

3.4 Basic Statistical Concepts and Choice of Distance Measure

In this section, we discuss some basic statistical concepts pertinent to this work. We next define the Kolmogorov–Smirnov distance, used to denote similarity between two images.

Fig. 8 Flowchart for method-I

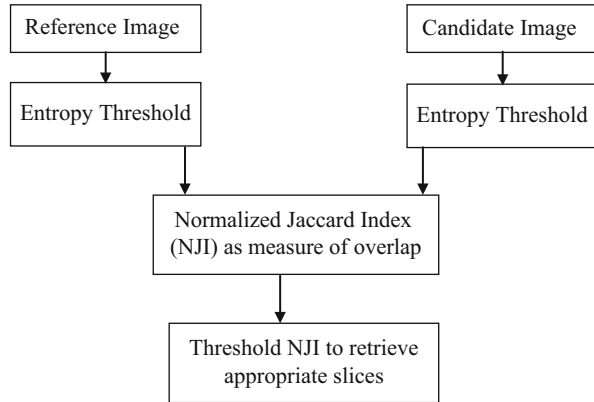
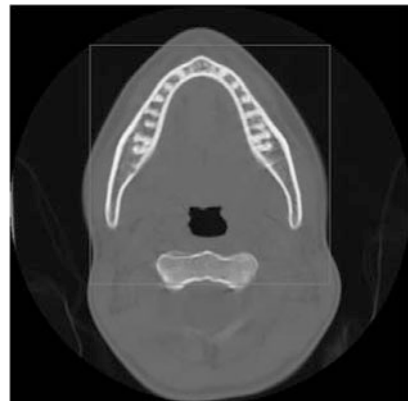


Fig. 9 Image in Fig. 4 with a selected area



Definition 4 If X is a discrete random variable, the function given by $f(x) = \Pr(X=x)$ for each x within the range of X is called the **probability distribution function** (pdf) of X .

Definition 5 The function which denotes the probability that a discrete random variable X takes on a value less than or equal to x is called the **cumulative distribution function** (cdf) of X .

Definition 6 **Kolmogorov–Smirnov (KS) distance** is defined as the largest difference (supremum) between two cdfs. Let X^c and Y^c , respectively, denote the cdfs of the distributions X and Y . Then, we can write [19]:

$$KS(X^c, Y^c) = \sup_i |X^c(i) - Y^c(i)| \tag{3}$$

We have essentially modeled image histograms as pdfs. So, Kullback–Leibler (KL) divergence or Jensen–Shannon (JS) divergence can be also employed as measures of similarity. However, it is often observed that cdfs are less sensitive

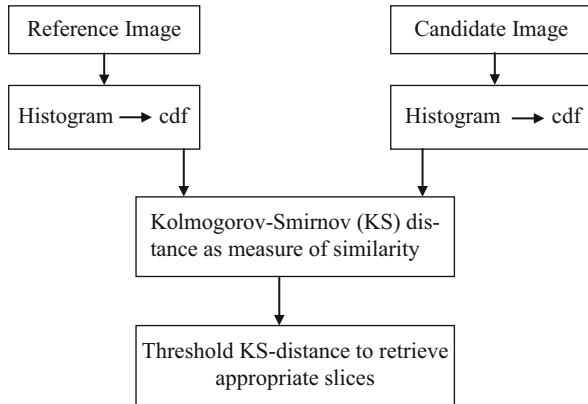


Fig. 10 Flowchart for method-II

to noise as compared to their pdf counterparts. So, we decide to use the cdf-based KS distance as a measure of similarity. It is important to note that the KS distance computation is based on nonparametric statistics, where we do not assume any particular form of a distribution [20].

3.5 Method-II: Image Retrieval Using Kolmogorov–Smirnov Distance

We now describe our second method (method-II) for the image retrieval. Here, we compute the similarity between the reference image (i.e., unbroken mandible) and the candidate images (2D slices in any input sequence) using *Kolmogorov–Smirnov* (KS) distance. The rationale behind the method is that two similar images exhibit a lower value of the KS distance as compared to two dissimilar images.

Figure 10 presents the flowchart for the second retrieval method. In this method, we first construct the histograms of the reference image and a candidate image. Since, a mandible has high intensity; we choose top 25 % of the intensity values, i.e. 192–255 for the construction of the histogram. We further consider the pixels only within a central region of interest and not in the entire image. We divide the above range of intensities to eight equal intervals of width eight pixels. Treating the above histograms as two *pdfs*, we construct the corresponding *cdfs*. Note that a very small interval for the histogram will make the *cdf* susceptible to noise. On the contrary, a very large interval will mask detailed intensity information. We choose an intermediate interval to address both these issues. This makes the *cdfs* less sensitive to noise without sacrificing detailed intensity information. From a pair of *cdfs*, *Kolmogorov–Smirnov* (KS) distance is computed. We finally threshold the *KS distances* to retrieve appropriate slices. Slices possessing values below the chosen threshold are retrieved.

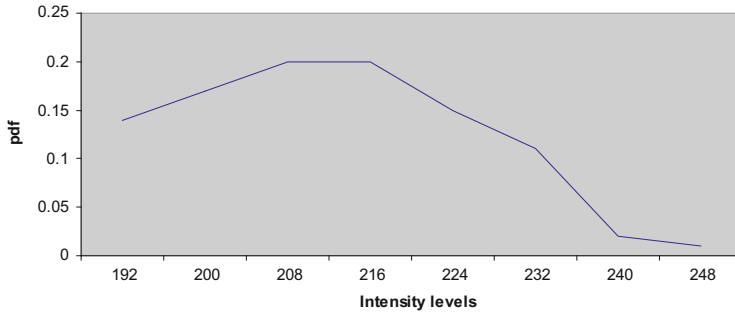


Fig. 11 Pdf of the histogram shown in Fig. 7

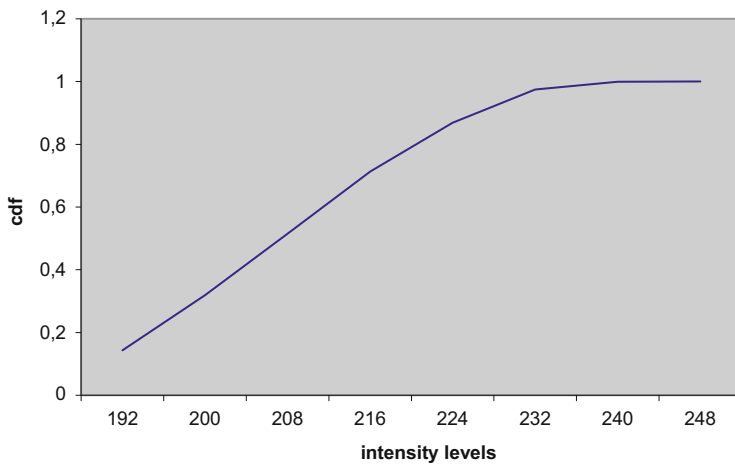


Fig. 12 Cdf of the pdf shown in Fig. 11

For the purpose of illustration, we now show the pdf (Figs. 11) and the corresponding cdf (Fig. 12) obtained from the histogram shown in Fig. 7. As mentioned above, we use an intensity range [192, 255] with eight equal intervals of eight pixels width.

4 Fracture Detection Using Max-Flow Min-Cut

Here, we first provide some basic concepts regarding flow networks. We next discuss the construction of the flow network for a 2D CT slice with suitable choices of vertices, edges, and capacity functions to be used as edge weights. We finally justify that the fracture detection problem can be modeled as identification of a minimum cut in the above flow network.

4.1 Network Flow Basics

We briefly state some useful definitions and an important theorem for the understanding of flow networks following [6].

Definition 7 A flow network $G = G(V, E)$ is a directed graph in which each edge $(u, v) \in E$ has a nonnegative capacity $c(u, v) \geq 0$. Two vertices in the flow network are distinguished as a source vertex s and a sink vertex t .

Definition 8 A cut (S, T) of a flow network $G = (V, E)$ is a partition of V into S and $T = V - S$ such that $s \in S$ and $t \in T$.

Definition 9 The capacity of a cut (S, T) is the sum of the capacities of the edges from S to T .

We next state the all important **Max-Flow Min-Cut theorem** without proof. For proof, please see [5, 6].

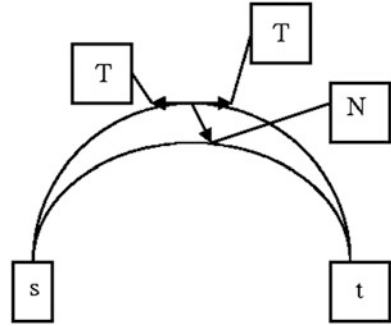
Theorem For any graph the maximum flow value from source vertex s to sink vertex t is equal to the minimal cut capacity of all cuts separating s and t .

4.2 Construction of Our Flow Network

A typical hairline fracture appears along the bone contours. So, we choose the set of boundary pixels P on the two mandibular contours (i.e., the inner and the outer contour) as the vertices of the proposed flow network $G = G(V, E)$. The two condyles, which are anatomical landmark points at the two terminals of the jaw, serve as the natural choices for the source vertex s and the sink vertex t . Thus, we can write: $V = P \cup \{s, t\}$. Since the boundary pixels for a mandible lie essentially on an arc, we construct *tangential* (T) and *normal* (N) edges in the proposed flow network representation. For each boundary pixel on a specific mandibular contour, we create edge links with the immediately forward and backward neighboring pixels. These constitute the T edges. On the other hand, the N edges are established between any two normal (or near-normal) boundary points across the two contours q and r . In addition, the first boundary pixel of both the contours q_f and r_f is attached to the source s and the last boundary pixel of both the contours q_l and r_l is attached to the sink t . So, we can write: $E = T \cup N \cup \{(q_f, s), (r_f, s), (q_l, t), (r_l, t)\}$. A typical flow network is shown below (Fig. 13):

The rationale of having tangential and normal neighbors is guided by the geometry of the mandible as well as by the fracture pattern. A typical hairline fracture appears along and also across the two mandibular contours. The tangential edges are appropriate for capturing a fracture along the contour and the normal edges are suitable for identifying a fracture across the contour. Let j and k be any two consecutive points along a mandibular contour with coordinates (x_j, y_j) and (x_k, y_k) , respectively. Then the equation of the line that is normal to the contour at point j is given by:

Fig. 13 A flow network with source s , sink t , tangential edges T and normal edges N



$$(x_k - x_j) x + (y_k - y_j) y + (x_j (x_j - x_k) + y_j (y_j - y_k)) = 0 \quad (4)$$

To be a normal neighbor to the point j , a point on the other contour should ideally satisfy Eq. (4). However, it is not always possible to find the exact normal neighbor (primarily due to sampling error). So, we compute the distance d_{jm} of a set of competing candidate points m having coordinates (m_x, m_y) and choose the one which yields the minimum value of d_{jm} . From basic coordinate geometry, we obtain:

$$d_{jm} = \frac{Am_x + Bm_y + C}{\sqrt{A^2 + B^2}} \quad (5)$$

where $A = (x_k - x_j)$, $B = (y_k - y_j)$, $C = (x_j(x_j - x_k) + y_j(y_j - y_k))$.

We choose a simple capacity function, with intensity and distance as its two parameters, as an edge weight between a pair of pixels. Let I_j and I_k be the intensities of two pixels j and k and let d_{jk} be the Euclidean distance between them. Then the capacity function c_{jk} is given by:

$$c_{jk} = \frac{I_j I_k}{d_{jk}} \quad (6)$$

We now provide an intuitive justification for the correctness of the proposed modeling of fracture detection as a minimum cut in an appropriately constructed flow network. From the discussion in the previous section, it is evident that every cut C in the flow network G satisfies following two properties [21]:

1. C groups the vertices of G into two disjoint sets
2. One set will contain the source vertex s and the other set will contain the sink vertex t

Now we justify the following claim with the max-flow min-cut theorem stated earlier.

Claim: A minimum cut C^* correctly identifies a fracture in the proposed 2D flow network G .

Justification: The justification is based on the max-flow min-cut theorem and the construction of the flow network with the capacity function given by Eq. (6). We seek to determine the maximum flow between s and t . Applying the above theorem, we obtain the minimum cut C^* . The minimum cut will consist of the cut edges in our flow network G . Basically, the cut edges are edges with comparatively low capacity values. From Eq. (6), it is evident that the low capacity edges are edges with relatively lower pixel intensity values and relatively higher distance values. These are exactly the characteristics of an edge in the vicinity of a fracture site. Note that since the broken fragments in a hairline fracture are not visibly out of alignment, a nonzero flow exists between them albeit with a lower value. The drop in the flow value is due to the presence of the fracture, which is a flow bottleneck in the constructed flow network. Thus, identification of a minimum cut C^* corresponds to detection of a fracture in the 2D flow network G . \square

The computation of the augmenting path is done using a *breadth-first-search*, as outlined in the *Edmonds–Karp* enhancement of the classical *Ford–Fulkerson* algorithm [6]. This algorithm has a worst-case time complexity $O(|V||E|^2)$, where $|V|$ denotes the cardinality of the vertex set V and $|E|$ denotes the cardinality of the edge set E in the flow network G .

5 Experimental Results

In this section, we present the experimental results with a detailed analysis. For implementation, we have used *ImageJ* [22], a public domain image-processing software, developed at National Institutes of Health (NIH), Bethesda, MD, USA. Five datasets with mandibles showing single hairline fracture, and one dataset with intact mandible are obtained from the Georgia Health Sciences University. The intact mandible is treated as the reference image. Each image in a dataset is of eight bit and has a dimension of 512×512 pixels. The resolution varies from 2.5 to 3.5 pixels/mm in various datasets. We first present the results for retrieval based on thresholding the NJI (Figs. 14 and 15) and KS distance (Figs. 16 and 17). We next show the results of actual detection of hairline fractures in some of the retrieved slices (Figs. 18 and 19).

For the purpose of illustration, four retrieved slices are shown for each dataset. For the NJI-based approach, retrieved images are those, whose binarized versions exhibit high similarity to the binarized version of the reference image. Similarity is computed from area of overlap measured using NJI. We have experimentally chosen the threshold value as 0.5. Slices with threshold values greater than 0.5 are retrieved. The threshold value, once chosen, is kept constant for all the datasets (Table 1). We show the mean and standard deviation of precision and recall values for this method in Table 2.

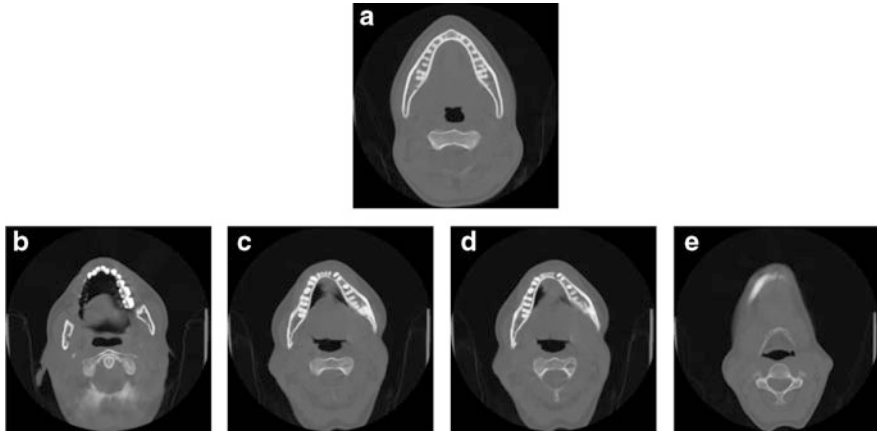


Fig. 14 Reference slice (a) and sample slices (b–e) from one dataset. Method-I retrieves (c) and (d)

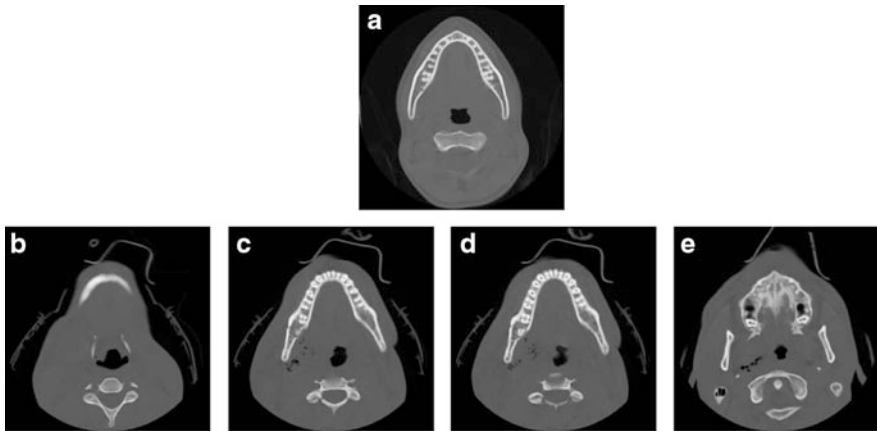


Fig. 15 Reference slice (a) and sample slices (b–e) from another dataset. Method-I retrieves (c) and (d)

For the KS distance-based approach also, the retrieved images are those, which exhibit high similarity with the reference image. However, similarity is computed in this case by estimating the distance between cdfs of the histograms with KS distance. We have experimentally chosen the threshold value to be 0.25. Slices with a threshold value smaller than 0.25 are retrieved. The threshold value, once chosen, is kept constant for all the datasets (Table 3). We show the mean and standard deviation of precision and recall values for this method in Table 4.

From Table 2, we see that method-I yields an average precision of 66.8 % and an average recall of 84.1 %. In contrast, Table 4 demonstrates that method-II has an average precision of 75.9 % and an average recall of 78.1 %. So, method-I

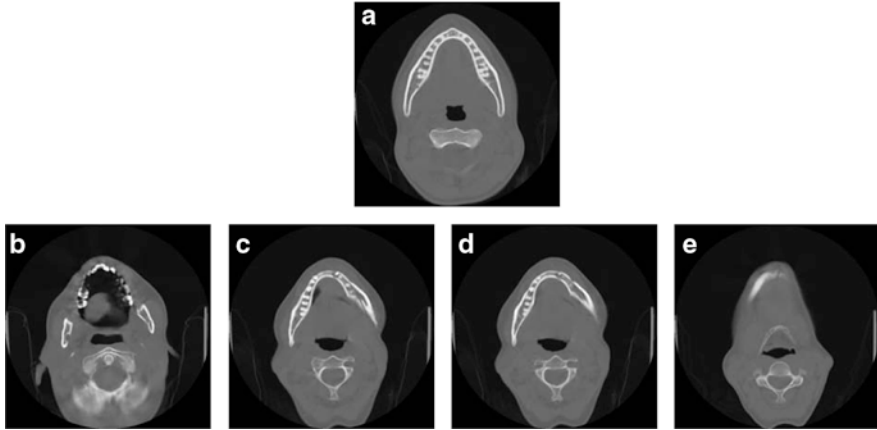


Fig. 16 Reference slice (a) and sample slices (b–e) from one dataset. Method-II retrieves (c) and (d)

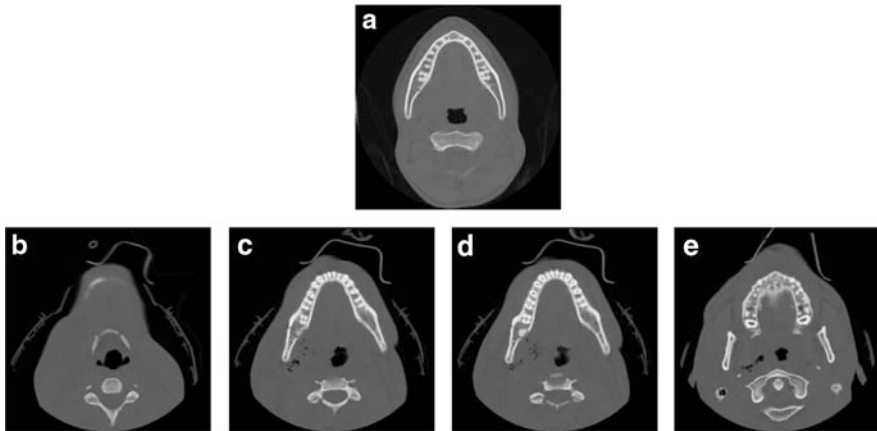


Fig. 17 Reference slice (a) and sample slices (b–e) from another dataset. Method-II retrieves (c) and (d)

has a lower value of precision but a higher value of recall compared to method-II. Method-I is less strict compared to method-II. So, in general, method-I retrieves a large number of slices. When more slices are retrieved, the chance of extracting a larger subset of the ground-truth, i.e., actual number of correct slices is higher. Thus, retrieval of more slices leads to an increase in the recall value. However, retrieval of large number of slices may contain more incorrect slices, which causes a decrease in the precision value. Method-II is more conservative than method-I, i.e., it retrieves lesser number of slices. So, chance of extracting a large number of incorrect slices is less, which in turn increases the precision value. However, extraction of lesser number of slices reduces the chance of retrieving a higher subset of ground-truth.

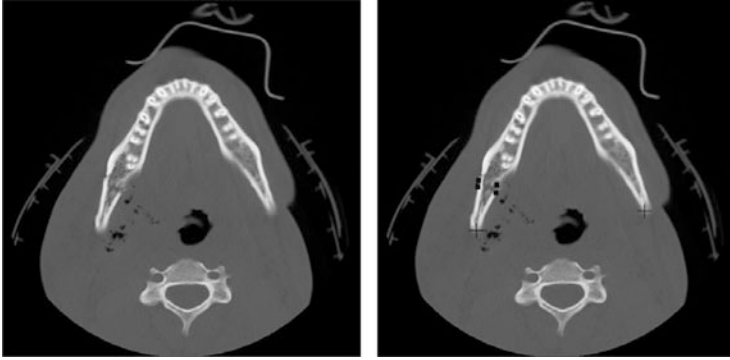


Fig. 18 Two-dimensional slice of a fractured mandible in the *left*. Fracture detection (*black squares*) with source and sink identification (*black crosses*) in the *right*

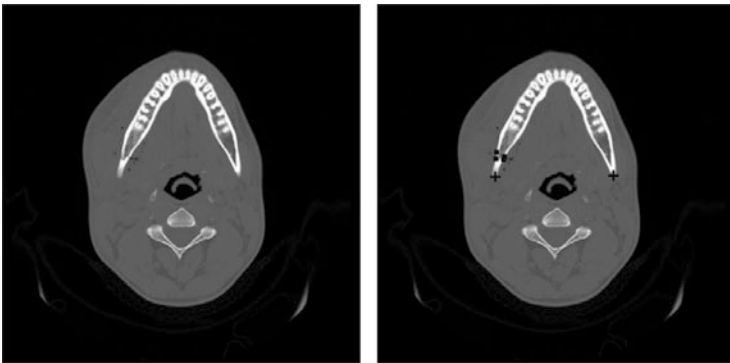


Fig. 19 Two-dimensional slice of a fractured mandible in the *left*. Fracture detection (*black squares*) with source and sink identification (*black crosses*) in the *right*

This leads to a fall in the value of recall. Now, we try to explain why method-I is less strict compared to method-II. Method-I estimates the overlap between the binarized versions of the reference image and a candidate image. Thus, it essentially involves comparison of just two intensities. But, method-II compares top 25 % of the intensity values between the reference image and a candidate image after modeling the respective histograms as cdfs.

Two different mandibles with the fracture sites identified are shown in Figs. 18 and 19. In each of these figures, the centers of the crosses mark the source vertex (in the left half of the image) and the sink vertex (in the right half of the image) and the fractures are indicated by dark squares. Upon execution of the max-flow min-cut algorithm, we obtain the edges in the cut set. Each such edge joins a vertex on the source-side with another vertex on the sink-side of the flow network. For

Table 1 Performance measure of method-I in terms of precision-recall values

Dataset	Retrieved slices (b)	Ground-truth slices (a)	Common slices (c)	Precision (%) ($100 \times c/b$)	Recall (%) ($100 \times c/a$)
I	14–21, 24–26, 29–39	25–39	25–26, 29–39	59.1	86.7
II	3–16	6–20	6–16	78.6	73.3
III	9–29, 36–40	8–27	9–27	73.1	95
IV	12–14, 17–38	10–30	12–14, 17–30	65.4	81
V	15–25, 35–37, 40–44	15–27	15–25	57.9	84.6

Table 2 Overall precision-recall value of method-I

Precision	66.8 ± 8.9
Recall	84.1 ± 7.9

Table 3 Performance measure of method-II in terms of precision-recall values

Dataset	Retrieved slices (b)	Ground-truth slices (a)	Common slices (c)	Precision (%) ($100 \times c/b$)	Recall (%) ($100 \times c/a$)
I	12–18, 25–37	25–39	25–37	65	86.7
II	1, 9–20	6–20	9–20	92.3	80
III	8–9, 13–23, 31, 39, 40	8–27	8–9, 13–23	81.3	65
IV	10,12, 14–25, 35–43	10–30	10, 12, 14–25	60.8	66.6
V	15–26, 42–44	15–27	15–26	80	92.3

Table 4 Overall precision-recall value of method-II

Precision	75.9 ± 12.9
Recall	78.1 ± 12.1

proper visualization, each such vertex is represented by a black square. Note that the slice in Fig. 18 is the one retrieved in Fig. 15c using method-I and Fig. 17c using method-II. The slice in Fig. 19 is from a different dataset (for which the retrieved slices are not shown). It is evident from the figures that the fractures are identified accurately in both cases. The ground-truth is obtained via manual detection by trained radiologists. We achieve a sensitivity of 79 % and a specificity of 59 % for the max-flow min-cut based fracture detection algorithm. The above values of sensitivity and specificity are due to (1) use of a simple capacity function during the min-cut and (2) use of only the intensity feature in the image retrieval procedure. The execution time for the max-flow min-cut algorithm is only few seconds on a 1.73 GHz Intel® Pentium® M Processor.

6 Conclusion and Future Scope

In this work, we discuss an automated detection of hairline fracture in mandibular images. Hairline fracture detection is a challenging problem as in many cases it can be missed by a practicing radiologist. The input to our problem is a sequence of CT images with scans of human craniofacial skeleton. A typical sequence consists of many slices out of which only a handful is observed to contain the fractured mandible. We first apply intensity-based image retrieval to identify the slices containing the fractured mandible. CT scan of an unbroken mandible is used as the reference image. Two different measures of similarity, namely the NJI and the Kolmogorov–Smirnov distance are used in this connection. We then model a hairline fracture as a minimum cut in an appropriately weighted flow network. The flow network is based on the geometry of the human mandible and some prior knowledge of the fracture pattern. A simple capacity function is used to compute the edge weights. The Edmonds–Karp enhanced Ford–Fulkerson algorithm is employed on the 2D flow network to obtain a minimum cut. The present work serves as an important tool for the radiologists and the craniofacial surgeons.

One direction of future work is to incorporate the shape information of the mandible in the retrieval process. A combination of shape and intensity information [23] and/or some new techniques like multi-texton histogram [24] can enhance the retrieval performance. In the present work, we have experimentally chosen the threshold values. However, based on statistical properties of the values of similarity measures, the thresholds can be properly selected. So, we plan to apply sophisticated statistical techniques like bootstrap [25] for selection of threshold. Finally, we will try to make the capacity function more robust by incorporating anatomical knowledge. For example, we can use the information that tissue swelling and specific low intensity regions called emphysema [26] typically appear in the vicinity of a mandibular fracture. All the aforementioned measures will increase the sensitivity and specificity values for computer-aided detection of hairline mandibular fractures.

References

1. King, R.E., Scianna, J.M., Petruzzelli, G.J.: Mandible fracture patterns: a suburban trauma center experience. *Am. J. Otolaryngol.* **25**(5), 301–307 (2004)
2. Ogunbare, B.O., Bonnick, A., Bayley, N.: Pattern of mandibular fractures in an urban major trauma center. *J. Oral Maxillofac. Surg.* **61**(6), 713–718 (2003)
3. Pashley, D.H., Borke, J.L., Yu, J.C.: Biomechanics and craniofacial morphogenesis. In: Lin, K.Y., Ogle, R.C., Jane, J.A. (eds.) *Craniofacial Surgery – Science and Surgical Technique*. Saunders, Philadelphia (2002)
4. Müller, H., Michoux, N., Bandon, D., Geissbuhler, A.: A review of content based image retrieval systems in medical applications – clinical benefits and future directions. *Int. J. Med. Inform.* **73**(1), 1–23 (2004)

5. Ford Jr., L.R., Fulkerson, D.R.: Maximum flow through a network. *Can. J. Math.* **8**, 399–404 (1956)
6. Cormen, T.H., Leiserson, C.E., Rivest, R.L., Stein, C.: *Introduction to Algorithms*. MIT Press, Cambridge (2001)
7. Kurihara, T.: The fourth dimension in simulation surgery for craniofacial surgical procedures. *Keio J. Med.* **50**(2), 155–165 (2001)
8. Siessegger, M., Schneider, B.T., Mischkowski, R.A., Lazar, F., Krug, B., Klesper, B., Zoller, J.E.: Use of an image-guided navigation system in dental implant surgery in anatomically complex operation sites. *J. Craniomaxillofac. Surg.* **29**(5), 276–281 (2001)
9. Chowdhury, A.S., Bhandarkar, S.M., Datta, G., Yu, J.C.: Automated detection of stable fracture points in computed tomography image sequences. In: *Proceedings of the Third IEEE International Symposium on Biomedical Imaging (ISBI)*, pp. 1320–1323, Arlington, 6–9 April 2006
10. Chowdhury, A.S., Bhattacharya, A., Bhandarkar, S.M., Datta, G., Yu, J.C., Figueroa, R.: Hairline fracture detection using MRF and Gibbs sampling. In: *Proceedings of the Eighth IEEE International Workshop on Applications of Computer Vision (WACV)*, p. 56, Austin (2007)
11. Hashimoto, T., Kuroda, S., Tanimoto, Y., Miyawaki, S., Takano-Yamamoto, T.: Correlation between craniofacial and condylar path asymmetry. *J. Oral Maxillofac. Surg.* **66**(10), 2020–2027 (2008)
12. Chowdhury, A.S., Bhandarkar, S.M., Robinson, R.W., Yu, J.C., Liu, T.: Detection of hairline mandibular fracture using max-flow min-cut and Kolmogorov–Smirnov distance. In: *Proceedings of the Eighth IEEE International Symposium on Biomedical Imaging (ISBI)*, pp. 1962–1965, Chicago (2011)
13. Rahman, M., Bhattacharya, P., Desai, B.C.: A framework for medical image retrieval using machine learning and statistical similarity matching techniques with relevance feedback. *IEEE Trans. Inf. Technol. Biomed.* **11**(1), 58–69 (2007)
14. Selvarani, A.G., Annadurai, S.: Content based image retrieval for medical images using generic Fourier descriptor. *J. Comput. Intell. Bioinform.* **1**(1), 65–72 (2008)
15. Sedghi, S., Sanderson, M., Clough, P.D.: A study on the relevance criteria for medical images. *Pattern Recognit. Lett.* **29**(15), 2046–2057 (2009)
16. Gonzalez, R.C., Woods, R.E.: *Digital image processing*. Addison-Wesley, Noida (2001)
17. Sahoo, P.K., Soltani, S., Wong, K.C., Chen, Y.C.: A survey of thresholding techniques. *Comput. Vis. Graph. Image Process.* **41**, 233–260 (1988)
18. Crum, W.R., Camara, O., Hill, D.L.G.: Generalized overlap measures for evaluation and validation in medical image analysis. *IEEE Trans. Med. Imaging* **25**(11), 1451–1461 (2006)
19. Chowdhury, A.S., Arabnia, H.R., Bandyopadhyay, D.: Improved stereo correlation using Moravec operator and Kolmogorov–Smirnov test. In: *Proceedings of the World Academy of Science International Conference on Computer Vision*, pp. 24–30, Las Vegas (2005)
20. Hollander, M., Wolfe, D.A.: *Nonparametric Statistical Methods*. Wiley, New York (1999)
21. Boykov, Y., Jolly, M.P.: Interactive graph cuts for optimal boundary & region segmentation of objects in N-D images. In: *IEEE International Conference on Computer Vision (ICCV)*, pp. 105–112, Vancouver (2001)
22. Rasband, W.S.: ImageJ, U. S. National Institutes of Health, Bethesda, MD. <http://imagej.nih.gov/ij/> (1997–2012)
23. Gevers, T., Smeulders, A.W.M.: PicToSeek: combining color and shape invariant features for image retrieval. *IEEE Trans. Image Process.* **9**(1), 102–119 (2000)
24. Liu, G.H., Zhang, L., Hou, Y.K., Li, Z.Y., Yang, J.Y.: Image retrieval based on multi-texton histogram. *Pattern Recognit.* **43**(7), 2380–2389 (2010)
25. Efron, B., Tibshirani, R.: *An Introduction to the Bootstrap*. Chapman & Hall, New York (1993)
26. Giannoudis, P.V., Dinopoulos, H.: Current concepts of the inflammatory response after major trauma: an update. *Injury* **36**(1), 229–230 (2005)